

MICROWAVE CONTINUUM EMISSION AND DENSE GAS TRACERS IN NGC 3627: COMBINING JANSKY VLA AND ALMA OBSERVATIONS

ERIC J. MURPHY¹, DILLON DONG², ADAM K. LEROY³, EMMANUEL MOMJIAN⁴, JAMES J. CONDON⁵, GEORGE HELOU⁶,
DAVID S. MEIER^{7,4}, JÜRGEN OTT⁴, EVA SCHINNERER⁸, JEAN L. TURNER⁹*Accepted to ApJ on July 7, 2021*

ABSTRACT

We present Karl G. Jansky Very Large Array (VLA) Ka band (33 GHz) and Atacama Large Millimeter Array (ALMA) Band 3 (94.5 GHz) continuum images covering the nucleus and two extranuclear star-forming regions within the nearby galaxy NGC 3627 (M66), observed as part of the Star Formation in Radio Survey (SFRS). Both images achieve an angular resolution of $\lesssim 2''$, allowing us to map the radio spectral indices and estimate thermal radio fractions at a linear resolution of $\lesssim 90$ pc at the distance of NGC 3627. The thermal fraction at 33 GHz reaches unity at and around the peaks of each HII region; we additionally observed the spectral index between 33 and 94.5 GHz to become both increasingly negative and positive away from the peaks of the HII regions, indicating an increase of non-thermal extended emission from diffusing cosmic-ray electrons and the possible presence of cold dust, respectively. While the ALMA observations were optimized for collecting continuum data, they also detected line emission from the $J = 1 \rightarrow 0$ transitions of HCN and HCO⁺. The peaks of dense molecular gas traced by these two spectral lines are spatially offset from the peaks of the 33 and 94.5 GHz continuum emission for the case of the extranuclear star-forming regions, indicating that our data reach an angular resolution at which one can spatially distinguish sites of recent star formation from the sites of future star formation. Finally, we find trends of decreasing dense gas fraction and velocity dispersion with increasing star formation efficiency among the three regions observed, indicating that the dynamical state of the dense gas, rather than its abundance, plays a more significant role in the star formation process.

Subject headings: galaxies: individual (NGC 3627) – galaxies: star formation – HII regions – ISM: molecules – radio continuum: general

1. INTRODUCTION

Stars form out of small pockets of dense molecular gas, with massive stars that are unambiguously young often embedded behind thick layers of dust. The dense star-forming gas is selectively traced by transitions with high critical densities, like the $J = 1 \rightarrow 0$ transitions of HCN or HCO⁺ (i.e., $n_{\text{crit}} \gtrsim 10^5 \text{ cm}^{-3}$). Likewise, recently formed stars are best studied by tracers such as free-free continuum at $\lambda \lesssim 1$ cm or hydrogen recombination-line tracers that are robust against extinction and selectively sensitive to the massive young stars that live only a short time after their birth. To constrain the complete physical process of star formation, ideally both tracers would be observed on scales matched to individual star-

forming regions. However, because of the faintness of both types of emission and the need for wide frequency coverage to isolate free-free emission from contaminants, this sort of study has been challenging before the current generation of radio and millimeter-wave telescopes, especially the Karl G. Jansky Very Large Array (VLA) and the Atacama Large Millimeter/submillimeter Array (ALMA). In this paper, we combined new observations from ALMA and the VLA to report one of the first extragalactic cloud-scale comparisons of dense gas, traced by the high effective density transitions HCN ($J = 1 \rightarrow 0$) and HCO⁺ ($J = 1 \rightarrow 0$), and recent star formation traced by $\lambda \lesssim 1$ cm free-free emission.

This paper represents the first results of a larger project to combine ALMA and the VLA to study continuum emission from nearby galaxies at frequencies ranging between 3 – 100 GHz. Emission at frequencies spanning 30 – 100 GHz is expected to be dominated by free-free emission from HII regions, providing a highly robust measure of massive star formation activity unbiased by dust. Unfortunately, this emission component is energetically weak, making detections difficult and time consuming even for bright objects. To date, observations in this frequency range have been largely limited to Galactic HII regions (e.g., Mezger & Henderson 1967), nearby dwarf irregular galaxies (e.g., Klein & Graeve 1986), galaxy nuclei (e.g., Turner & Ho 1983, 1994), nearby starbursts (e.g., Klein et al. 1988; Turner & Ho 1985), and super star clusters within nearby blue compact dwarfs (e.g., Turner et al. 1998; Kobulnicky & Johnson 1999). However, with ALMA now online, 3 mm bolometer arrays

¹ Infrared Processing and Analysis Center, California Institute of Technology, MC 314-6, Pasadena, CA 91125, USA; emurphy@ipac.caltech.edu

² Department of Physics and Astronomy, Pomona College, Claremont, CA 91711, USA

³ The Ohio State University, 140 W18th St, Columbus, OH 43210, USA

⁴ National Radio Astronomy Observatory, P.O. Box O, 1003 Lopezville Road, Socorro, NM 87801, USA

⁵ National Radio Astronomy Observatory, 520 Edgemont Road, Charlottesville, VA 22903, USA

⁶ California Institute of Technology, MC 100-22, Pasadena, CA 91125, USA

⁷ New Mexico Institute of Mining & Technology, 801 Leroy Place, Socorro, NM 87801, USA

⁸ Max Planck Institut für Astronomie, Königstuhl 17, Heidelberg D-69117, Germany

⁹ Department of Physics and Astronomy, UCLA, Los Angeles, CA 90095, USA

Table 1
Source Names and Imaging Summary

| Source | R.A. (J2000) | Decl. (J2000) | Beam (33 GHz) | $\sigma_{33 \text{ GHz}}$ ($\mu\text{Jy bm}^{-1}$) | Beam (94.5 GHz) | $\sigma_{94.5 \text{ GHz}}$ ($\mu\text{Jy bm}^{-1}$) |
|------------------|-----------------|------------------|------------------------|---|------------------------|---|
| NGC 3627 | 11 20 15.0 | +12 59 30 | $2''.83 \times 1''.83$ | 26 | $1''.89 \times 1''.66$ | 32 |
| NGC 3627 Enuc. 1 | 11 20 16.2 | +11 20 16 | $2''.45 \times 2''.03$ | 20 | $1''.88 \times 1''.67$ | 32 |
| NGC 3627 Enuc. 2 | 11 20 16.3 | +11 20 16 | $2''.55 \times 2''.08$ | 25 | $1''.89 \times 1''.67$ | 32 |

such as MUSTANG (Dicker et al. 2008), along with recent improvements to the backends of existing radio telescopes, such as the Caltech Continuum Backend (CCB) on the Robert C. Byrd Green Bank Telescope (GBT) and the Wideband Interferometric Digital ARchitecture (WIDAR) correlator on the VLA, the availability of increased bandwidth is making it possible to conduct investigations for larger samples of extragalactic objects at frequencies $\gtrsim 30$ GHz (e.g., Murphy et al. 2011, 2012; Nikolic & Bolton 2012).

Taking advantage of this new capability, the Star Formation in Radio Survey (SFRS; see Murphy et al. 2012), targets 118 star-forming regions (56 nuclear and 62 extranuclear) in 56 nearby galaxies ($d < 30$ Mpc) that had been observed at infrared (IR) and optical wavelengths as part of the SINGS (Kennicutt et al. 2003) and KINGFISH (Kennicutt et al. 2011) legacy programs. Of these, 112 (50 nuclei and 62 extranuclear regions) have $\delta > -35^\circ$ and are thus observable with the VLA, while 54 are observable with ALMA (i.e., $\delta < 30^\circ$). We observed 9 of these regions at frequencies near 95 GHz using ALMA’s Band 3 receiver during the second early science campaign (“Cycle 1”). All 9 of these targets had already been observed by the VLA.

Thanks to ALMA’s strong multiplexing capabilities and excellent sensitivity, we were also able to make a simultaneous search for bright line emission near 95 GHz. Specifically, the bandpass always covers the rest-frame $J = 1 \rightarrow 0$ transition of HCO^+ and often includes the $J = 1 \rightarrow 0$ transition of HCN. These are two of the standard extragalactic tracers of dense molecular gas (Gao & Solomon 2004; Graciá-Carpio et al. 2006). Thus our combined VLA and ALMA observations yield an unbiased view of the ionizing radiation emitted by massive young stars and a snapshot of the kind of bright, dense structure that might give birth to these regions.

In this paper, we report on the combination of VLA and ALMA data for three regions in the nearby galaxy NGC 3627 (M66), having a kinematic local standard of rest velocity $v_{\text{LSRK}} = 726 \pm 3 \text{ km s}^{-1}$. Along with NGC 3628 and NGC 3623, NGC 3627 makes up the well-known Leo Triplet galaxy group. It is classified with a morphological type of SABb¹, located at a distance of 9.38 ± 0.35 Mpc (Freedman et al. 2001), and hosts a Seyfert 2 AGN (Ho et al. 1997; Moustakas et al. 2010). An H I plume extending $\approx 50'$ indicates that the two largest spirals in the group, NGC 3627 and 3628, have interacted in the past (e.g., Haynes et al. 1979). NGC 3627 has comparable amounts of atomic and molecular gas (Helfer et al. 2003; Walter et al. 2008), which is a rather high molecular gas fraction compared to other local star-

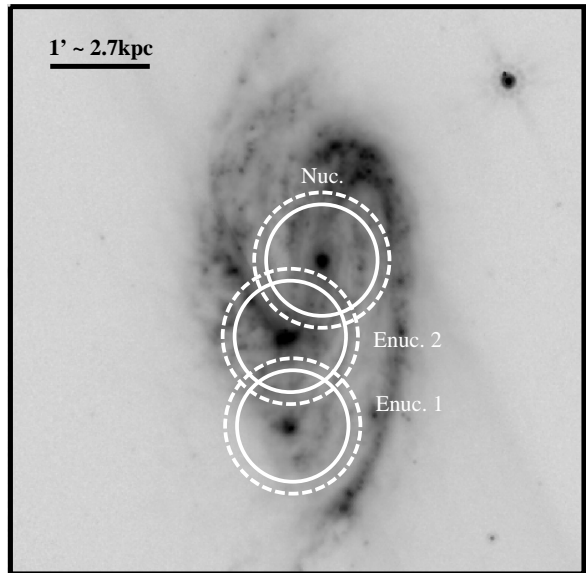


Figure 1. The locations of the VLA (dashed line) and ALMA (solid line) pointings for each region in NGC 3627 overlaid on a *Spitzer* $\lambda = 8 \mu\text{m}$ grayscale image. The circles outline the FWHMs of the VLA and ALMA primary beams at 33 and 94.5 GHz, respectively.

forming galaxies (e.g., Saintonge et al. 2011). It has been suggested that the high $\text{H}_2/\text{H I}$ mass ratio in NGC 3627 is the result of the tidal interaction with NGC 3628, since this galaxy has stripped much of the H I originally in NGC 3627 (Zhang et al. 1993).

The paper is organized as follows: In §2 we describe the data as well as the analysis procedures used in the present study. In §3 we present our results and discuss their implications. Our main conclusions are then summarized in §4.

2. DATA AND ANALYSIS

We targeted the nucleus and two extranuclear star-forming regions in NGC 3627 with both ALMA and the VLA (Table 1), achieving a common resolution of $\approx 2''$, which is ≈ 90 pc at the distance of NGC 3627. In Figure 1 we identify the locations of each region targeted in NGC 3627, showing the full width at half maximum (FWHM) of the VLA and ALMA primary beams at 33 and 94.5 GHz on a *Spitzer* $\lambda = 8 \mu\text{m}$ greyscale image. The fields were selected to target individual massive star-forming regions, and the $\lambda = 8 \mu\text{m}$ image shows that each field is centered on a substantial concentration of bright polycyclic aromatic hydrocarbon (PAH) emission, indicating a combination of intense radiation and abundant small dust grains. For the case of NGC 3627, this yields a sample that includes the nuclear disk, an isolated H II region (Enuc. 1), and the star-forming complex at the end

¹ Kinematic LSR velocity and morphological type taken from the NASA Extragalactic Database (NED; <http://nedwww.ipac.caltech.edu>).

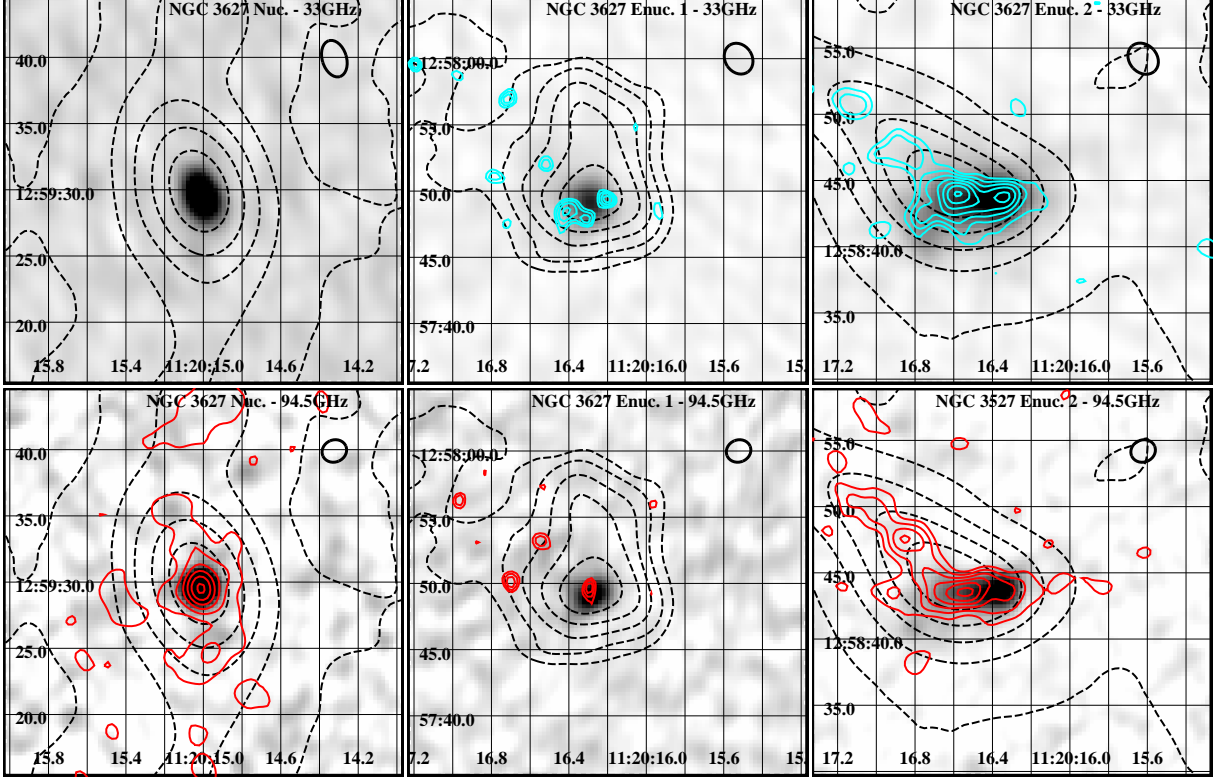


Figure 2. Continuum images of the three regions at 33 and 94.5 GHz are shown in the first and second rows, respectively. Coordinates are in J2000. The restoring beam size (FWHM) is illustrated in the upper right corner of each panel. At the distance of NGC 3627, $1''$ linearly projects to ≈ 45.5 pc on the sky. CO contours are overlaid on each grayscale image as black dashed lines. The resolution of the CO images is far lower than in our ALMA or VLA images, being $7.3'' \times 5.8''$. HCN contours (cyan) are overlaid on the 33 GHz grayscale images in the *top* three panels, while HCO^+ contours (red) are overlaid on the 94.5 GHz grayscale images in the *bottom* three panels. In all cases, contour lines are drawn using a linear scaling starting from the 2σ value. As discussed in the text, the full velocity range of HCN emission towards the nucleus is cutoff by the bandpass at $v_{\text{LSRK}} \approx 800 \text{ km s}^{-1}$, and therefore not shown.

of a bar (Enuc. 2), allowing us to compare star formation and molecular gas properties for three very different environmental conditions.

We worked with four data sets: VLA continuum observations at Ka band (29–37 GHz), ALMA continuum observations centered at ≈ 95 GHz, ALMA line observations of the $J = 1 \rightarrow 0$ transition of HCO^+ and HCN, and archival BIMA Survey of Nearby Galaxies (SONG Helfer et al. 2003) line observations of the $J = 1 \rightarrow 0$ transition of CO.

2.1. VLA Ka-Band Data

Details on all of the SFRS VLA Ka-band survey observations and data reduction can be found in E.J. Murphy et al. (2015, in preparation). Here, we present data only for NGC 3627. D-configuration observations were obtained in November 2011 (VLA/11B-032) and March 2013 (VLA/13A-129). For the first round of observations, the 8-bit samplers were available, yielding 2 GHz of simultaneous bandwidth, which we used to center 1 GHz wide sub-bands at 32.5 and 33.5 GHz. For the latter run, the 3-bit samplers became available, yielding 8 GHz of instantaneous bandwidth in 2 GHz wide sub-bands centered at 30, 32, 34, and 36 GHz. In both cases, 3C 286 was used as the flux density and bandpass calibrator, while J 1118+1234 was used as the complex gain and telescope pointing calibrator. To reduce the VLA data, we used the Common Astronomy Software Appli-

cations (CASA; McMullin et al. 2007) and followed standard procedures.

2.2. ALMA Band-3 Data

In December 2013 as part of ALMA’s Cycle 1 observing campaign, we obtained data for a subset of 9 SFRS sources chosen to be sufficiently bright at $24 \mu\text{m}$ and close enough on the sky that multiple sources could be observed in a single scheduling block. The array configuration was chosen to match the $\lesssim 2''$ synthesized beam of the VLA 33 GHz data. While the goal of the ALMA observing program is to deliver continuum images at ≈ 95 GHz, we set the local oscillator frequency to 94.5 GHz, centering the four 1.875 GHz wide spectral windows at 87.5, 89.5, 99.5, and 100.5 GHz, to cover the rest frequencies of HCN ($J = 1 \rightarrow 0$)/88.6318 GHz, HCO^+ ($J = 1 \rightarrow 0$)/89.1885 GHz, HNC ($J = 1 \rightarrow 0$)/90.6636 GHz, and $\text{H}40\alpha$ /99.0229 GHz. Like the VLA data, the ALMA data were reduced and calibrated using CASA following standard procedures as part of the ALMA quality assurance process. Here we present the nucleus and two extranuclear star-forming region in NGC 3627. The remaining ALMA sources, along with corresponding VLA data, will be presented together in a forthcoming paper.

2.3. Archival CO ($J = 1 \rightarrow 0$) Data

To investigate how the amount of dense star-forming gas compares to the total molecular gas reservoir, we

Table 2
VLA and ALMA Continuum Properties

| Source | R.A. (J2000) | Decl. (J2000) | S_P (mJy bm ⁻¹) | S_I (mJy) | $\theta_M \times \theta_m$ | T_b (K) |
|---------------------|-----------------|------------------|----------------------------------|-----------------|--|-------------------|
| 33 GHz Components | | | | | | |
| NGC 3627 | 11 20 15.01 | +12 59 29.5 | 1.70 ± 0.06 | 2.09 ± 0.08 | $1''.21 \pm 0''.15 \times 0''.97 \pm 0''.10$ | 1.98 ± 0.34 |
| NGC 3627 Enuc. 1 | 11 20 16.30 | +12 57 49.1 | 0.77 ± 0.03 | 1.66 ± 0.09 | $2''.52 \pm 0''.23 \times 2''.25 \pm 0''.27$ | 0.33 ± 0.05 |
| NGC 3627 Enuc. 2 | 11 20 16.46 | +12 58 43.5 | 0.98 ± 0.04 | 5.35 ± 0.27 | $6''.95 \pm 0''.30 \times 3''.12 \pm 0''.17$ | 0.28 ± 0.02 |
| 94.5 GHz Components | | | | | | |
| NGC 3627 | 11 20 15.02 | +12 59 29.6 | 1.22 ± 0.07 | 1.58 ± 0.11 | $1''.10 \pm 0''.16 \times 0''.77 \pm 0''.29$ | 0.252 ± 0.102 |
| NGC 3627 Enuc. 1 | 11 20 16.29 | +12 57 49.2 | 0.63 ± 0.05 | 1.13 ± 0.11 | $1''.95 \pm 0''.24 \times 1''.24 \pm 0''.22$ | 0.063 ± 0.015 |
| NGC 3627 Enuc. 2 | 11 20 16.44 | +12 58 43.5 | 0.68 ± 0.05 | 3.23 ± 0.25 | $5''.66 \pm 0''.36 \times 1''.85 \pm 0''.15$ | 0.042 ± 0.005 |

make use of $J = 1 \rightarrow 0$ CO data taken as part of the BIMA SONG survey (Helfer et al. 2003). The rms noise of the CO channel map is 41 mJy bm⁻¹ in a 10 km s⁻¹ channel. The resolution of the CO map is significantly coarser than our ALMA and VLA data, having a synthesized beam of $7''.3 \times 5''.8$.

2.4. Continuum Imaging and Photometry

Calibrated VLA and ALMA measurement sets for each source were imaged using the task CLEAN in CASA. The Ka-band images contain data from both sets of observations, but are heavily weighted by the 13A semester observations as those include significantly more data. The mode of CLEAN was set to multifrequency synthesis (MFS; Conway et al. 1990; Sault & Wieringa 1994). We chose to use *Briggs* weighting with ROBUST=0.5, and set the variable NTERMS=2, which allows the cleaning procedure to also model the spectral index variations on the sky. To help deconvolve extended low-intensity emission, we took advantage of the multiscale clean option (Cornwell 2008; Rau & Cornwell 2011) in CASA, searching for structures with scales ≈ 1 and 3 times the FWHM of the synthesized beam. A primary beam correction was applied using the CASA task IMPBCOR before analyzing the images. The primary-beam-corrected continuum images at 33 and 94.5 GHz for each of the three targeted sources are shown in Figure 2. The synthesized beamwidths and rms noises of each image are given in Table 1. We also note that the largest angular scales that the ALMA and VLA images should be sensitive to are $\approx 25''$ and $44''$, respectively.

To measure the integrated flux densities and source sizes from each field, we used the task IMFIT in CASA to fit sources within a circular aperture having a radius of $15''$. In Table 2 we list the deconvolved source parameters from IMFIT, including the positions of the source components, peak brightnesses (S_P), integrated flux densities (S_I), deconvolved source sizes ($\theta_M \times \theta_m$), and corresponding brightness temperatures (T_b). In addition to the errors reported by IMFIT, the uncertainties on the peak brightnesses and integrated flux densities include the contribution from image rms, as well as an absolute calibration uncertainty of 3% at 33 GHz (Perley & Butler 2013) and 5% at 94.5 GHz (ALMA Cycle 1 Technical Handbook), which in fact dominates the uncertainties. Clearly for the case of Enuc.2, which is an elongated structure at the end of the bar, a single-component fit is not the most appropriate.

2.5. Line Imaging and Photometry

We detected the $J = 1 \rightarrow 0$ lines of HCN and HCO⁺ towards each targeted region in NGC 3627. We did not detect H40 α for any of the targeted regions, and our frequency coverage missed HNC ($J = 1 \rightarrow 0$) in each case. Similar to the continuum imaging, the line data were imaged using the task CLEAN in CASA. However, before the line images were created, the data were first continuum subtracted using the CASA task UVCONTSUB. The rms noise of the ALMA channel maps is ≈ 1.2 mJy bm⁻¹ in a 10 km s⁻¹ channel.

Moment 0 maps were constructed by integrating the spectra at each pixel of the spectral cubes. These are overlaid on the continuum maps in Figure 2. Unfortunately, the detection of HCN towards the nucleus is cut off by the bandpass at a radial velocity of $v_{\text{LSRK}} \approx 800$ km s⁻¹. The moment 0 map for HCO⁺ towards the nucleus shows that we are missing higher velocity HCN emission to the north. This can also be seen in Figure 3, which shows the spectra of both HCN and HCO⁺ for all targeted regions. The spectra were extracted using a circular aperture centered on the 94.5 GHz source positions returned by IMFIT having a diameter that was 20% larger than the corresponding source size major axis convolved with the 94.5 GHz beam. We therefore exclude the nuclear HCN line emission in this study. For all other regions in Figure 3, the HCN and HCO⁺ line profiles are fit by a Gaussian. The corresponding velocity dispersions are given in each panel, along with uncertainties that were estimated using the errors per channel along with a Monte Carlo approach.

Given that the CO ($J = 1 \rightarrow 0$) image has a much coarser angular resolution than our ALMA line images, we must first convolve our images to the resolution of the CO map before estimating dense molecular gas fractions. This must similarly be done for the continuum (33 and 94.5 GHz) data for estimating star formation efficiencies (see §3.3). The resolution matching was carried out using the task IMSMOOTH in CASA, before re-gridding each image to a common pixel scale. For such measurements requiring the convolved data, photometry was carried out by simply taking the peak brightness within a circular aperture having a radius of $15''$ (see Table 3), as this provides a way to mitigate any differences in our comparisons that may arise from being observed with different interferometers having different sensitivities on different spatial scales.

3. RESULTS AND DISCUSSION

Table 3
Photometry Incorporating CO Data

| Source | I_{CO} (K Km s ⁻¹) | I_{HCN} (K Km s ⁻¹) | I_{HCO^+} (K Km s ⁻¹) | $S_{33 \text{ GHz}}$ (mJy bm ⁻¹) |
|------------------|--|---|---|---|
| NGC 3627 | 375.47 ± 19.3 | 4.54 ± 0.48 | 13.80 ± 0.81 | 2.10 ± 0.06 |
| NGC 3627 Enuc. 1 | 48.19 ± 4.4 | 1.05 ± 0.23 | 0.50 ± 0.20 | 1.56 ± 0.05 |
| NGC 3627 Enuc. 2 | 263.03 ± 13.6 | 6.62 ± 0.46 | 7.15 ± 0.47 | 3.38 ± 0.10 |

Note. — Photometry was carried out after convolving both VLA and ALMA maps to the 7''.3 × 5''.8 synthesized beam of the BIMA SONG $J = 1 \rightarrow 0$ CO data.

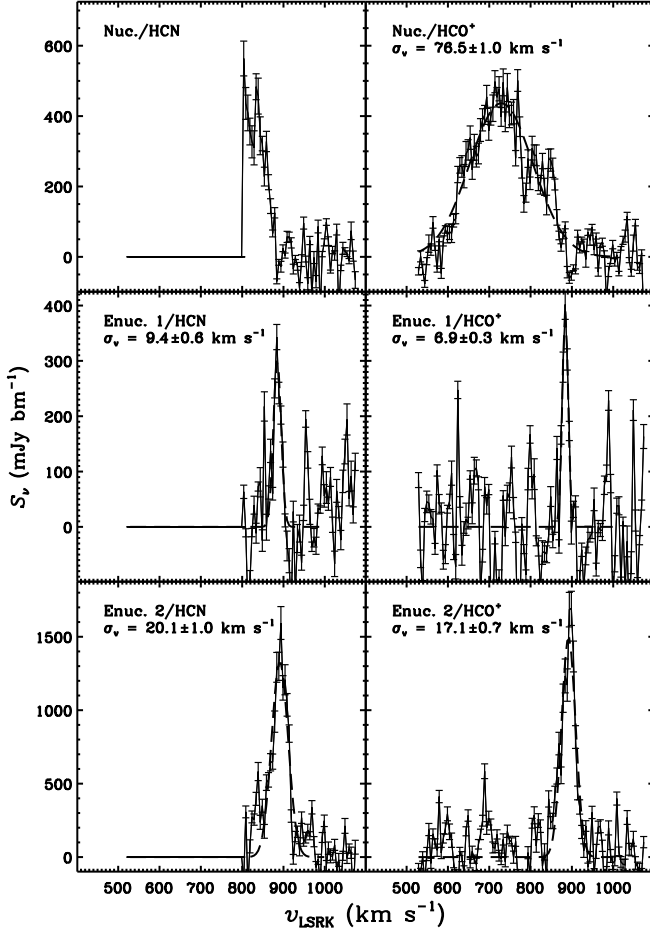


Figure 3. HCN and HCO⁺ spectra (5 km s⁻¹ channels) for each of the three targeted regions within NGC 3627 extracted using a circular aperture centered on the 94.5 GHz source positions returned by IMFIT. The diameter of each aperture was 20% larger than the corresponding source size major axis convolved with the 94.5 GHz beam. The full velocity range of HCN emission towards the nucleus is cutoff by the bandpass at $v_{\text{LSRK}} \approx 800$ km s⁻¹. For all other regions, the spectral lines are fit by Gaussians (dashed lines), and the corresponding fitted velocity dispersions and uncertainties are given in the upper left corner of each panel.

In the following section we present our results along with a brief discussion about their implications for the star-formation activity in the three regions observed in NGC 3627.

3.1. Spectral Indices and Thermal Radio Fractions

We created a 33-to-94.5 GHz spectral-index map (i.e., α , where $S_\nu \propto \nu^\alpha$) of each source after convolving the slightly higher resolution 94.5 GHz data to match the beam of the 33 GHz data and putting the data on the

same grid. In the top panels of Figure 4 the spectral indices are overlaid on 94.5 GHz continuum images for which pixels not detected at the 3σ level have been clipped. Focusing only on the regions (i.e., pixels) detected at $> 3\sigma$ in each map, we measured mean spectral indices of $\alpha_{33 \text{ GHz}}^{94.5 \text{ GHz}} = -0.10, -0.15$, and -0.27 for the nucleus and extranuclear regions 1 and 2, respectively. The corresponding standard deviations over these regions are 0.20, 0.18, and 0.15, respectively. As expected, these are relatively flat, being < -0.5 for each discrete source. We note that the spectral indices in some cases become positive in the outskirts of the HII regions, which may indicate a significant contribution of thermal dust to the 94.5 GHz emission, although the uncertainties on the spectral indices in the HII region outskirts become large.

If we assume a fixed non-thermal spectral index for each source, we can use the measured spectral indices to estimate the fractional contributions from thermal emission (e.g., Klein et al. 1984; Murphy et al. 2012). While most sensitive to the assumption of the non-thermal spectral index, this simple thermal decomposition also assumes that the free-free emission does not become optically thick at $\nu \gtrsim 30$ GHz (e.g., Murphy et al. 2010b), and that there is an insignificant contribution of anomalous microwave emission at ~ 33 GHz (e.g., Murphy et al. 2010a) and thermal dust emission at ~ 94.5 GHz. As discussed below, the few regions where there may be evidence for thermal dust emission are excluded from the thermal fraction calculations. We took the non-thermal spectral index to be $\alpha^{\text{NT}} = -0.85$, which is the average non-thermal spectral index found among the 10 star-forming regions studied in NGC 6946 by Murphy et al. (2011) and very similar to the average value found by Niklas et al. (1997, i.e., $\alpha^{\text{NT}} = -0.83$ with a scatter of $\sigma_{\alpha^{\text{NT}}} = 0.13$) globally for a sample of 74 nearby galaxies. The 33 GHz thermal fraction contours are overlaid on the 33 GHz continuum images in the bottom panels of Figure 4, indicating thermal fractions near unity on the peaks of the continuum emission.

While NGC 3627 is known to host an AGN, the AGN does not appear to contribute significantly to the radio continuum emission. Filho et al. (2004) reported a 5 GHz flux density of < 0.3 mJy within a $3.6 \text{ mas} \times 1.4 \text{ mas}$ beam using the VLBA. Scaling this to 33 GHz assuming a non-thermal spectral index of $\alpha^{\text{NT}} = -0.85$ results in an estimated AGN contribution to the 33 GHz emission of $< 60 \mu\text{Jy}$, or $< 3\%$ of the integrated 33 GHz emission for the nuclear component reported by IMFIT (see §2.4). We therefore assume that the nuclear emission is primarily powered by star formation in the rest of the analysis.

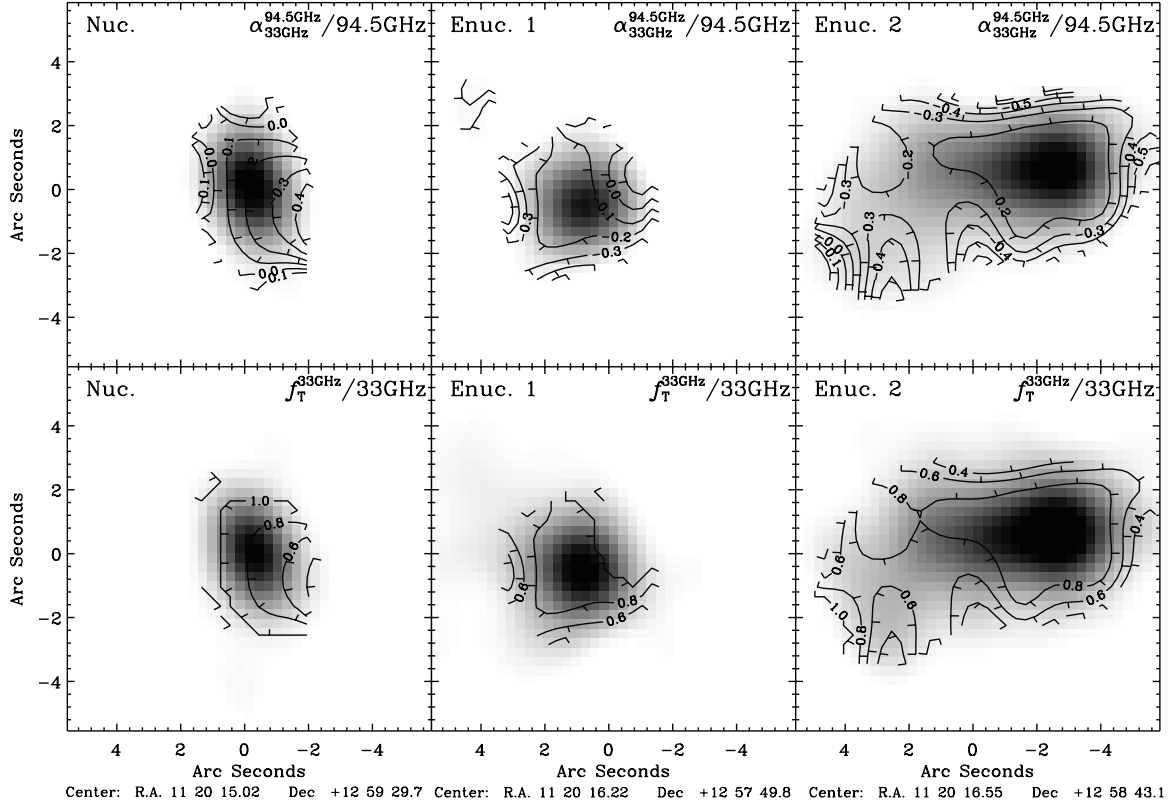


Figure 4. *Top row:* Spectral index contours between 33 and 94.5 GHz overlaid on the 94.5 GHz continuum image of the nucleus (left), Enuc. 1 (middle), and Enuc. 2 (right). In each case, the spectral indices flatten at the peaks of the continuum emitting regions. *Bottom row:* Estimated thermal fractions at 33 GHz overlaid on the 33 GHz continuum image of the nucleus (left), Enuc. 1 (middle), and Enuc. 2 (right) of NGC 3627. For both extranuclear star-forming regions, the 33 GHz thermal fractions approach unity on the peaks of the continuum emitting regions.

Ignoring those regions for which the spectral index was measured to be flatter than $\alpha_T = -0.1$ by more than 1σ , where there may be a contribution from thermal dust, we measure corresponding mean 33 GHz thermal fractions over the nucleus, Enuc. 1 and 2 of 85, 82 and 70%, respectively. The corresponding standard deviations measured over these regions are 19, 19 and 20%. The thermal fraction distribution and average values are in agreement with the results presented by Murphy et al. (2012), who reported an average 33 GHz thermal fraction of $\approx 76\%$ with a dispersion of 24% for their entire sample, and even higher values (i.e., $>90\%$, on average) for all sources resolved on scales of $\lesssim 500$ pc. We note that assuming a much flatter non-thermal spectral index has little effect on the estimated thermal fraction given the flat spectral indices measured between 33 and 94.5 GHz. For example, by instead assuming $\alpha^{\text{NT}} = -0.6$, the mean 33 GHz thermal fractions over the nucleus, Enuc. 1, and 2 are 80, 76, and 62%, respectively, which are well within the quoted standard deviations.

3.2. Spatial Offsets Between Continuum and Line Emission

One of the most obvious results from an inspection of the maps in Figure 2 is the spatial offset between the peaks of the continuum and line emission. This is especially evident for Enuc. 2 (i.e., the bar end) for which both dominant HCN and HCO^+ peaks are well to the east of the 33 and 94.5 GHz continuum peaks. The continuum and molecular gas are spatially offset in the plane

of the sky by $\approx 3''$ (≈ 130 pc at the distance of NGC 3627).

The critical density of both the $J = 1 \rightarrow 0$ lines of HCN and HCO^+ is $n_{\text{crit}} \gtrsim 10^5 \text{ cm}^{-3}$, and thus probes the densest, UV-shielded gas that is likely in the process of, or soon will be, forming stars. Assuming that the 33 and 94.5 GHz continuum is primarily powered by free-free emission, as suggested by the results presented in §3.1, and thus robustly traces ongoing star formation that is $\lesssim 10$ Myr old, this offset suggests that we have reached the spatial resolution at which we can reliably separate the fuel stockpiles from the current generation of star formation.

Pan et al. (2013) similarly report ~ 100 pc offsets between peaks of dense gas (HCN $J = 1 \rightarrow 0$) and star formation (3 cm radio continuum) in the starburst ring of the barred galaxy NGC 7522. These authors suggest that dense-gas formation is promoted by gas cloud collisions at the intersections between the galaxy bar and ring orbits, and that offsets between the dense gas peaks and those of ongoing star formation occur farther downstream from the orbit contact points. Similar conclusions have also been found for nuclear bars in nearby starbursts (e.g., Meier et al. 2008). Like NGC 7522, NGC 3627 is a barred galaxy with an inner molecular ring (Regan et al. 2002), suggesting that similar dynamics may also be driving the formation of dense gas and its observed spatial offsets from the peaks of ongoing star formation activity in Enuc. 2.

Assuming this scenario to be true, we can make a rough estimate of the propagation time between the newly

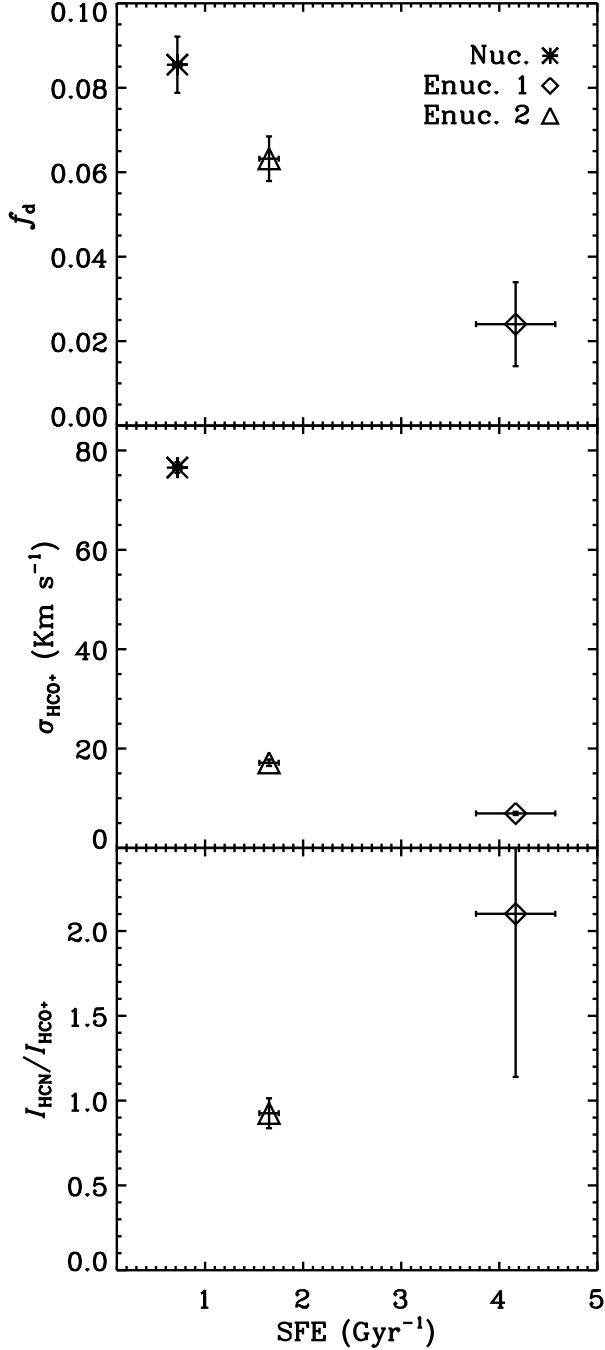


Figure 5. *Top:* Dense gas fraction f_d plotted as a function of star formation efficiency for each region observed in NGC 3627. The quantities on the two axes are both normalized by CO luminosity and so some spurious correlation is expected in the presence of noise. However, to the contrary we observe an anti-correlation between star formation efficiency and dense gas fraction, which is opposite the sense expected from only noisy CO measurements. *Middle:* HCO^+ velocity dispersions from the fitted line profiles shown in Figure 3 plotted as a function of star formation efficiency for each region observed in NGC 3627. *Bottom:* Ratio of HCN to HCO^+ brightnesses plotted against star formation efficiency, indicating a trend of increasing line brightness ratio with increasing measure of ionizing photons per unit molecular gas mass. Given that we are missing higher velocity HCN emission to the north of the nucleus, this data point is omitted in the bottom panel.

formed stars, as traced by the free-free radio continuum emission, and the dense gas peaks. The rotation speed of

the NGC 3627's disk at the distance to the bar end (i.e., $\approx 100'' \approx 4.5 \text{ kpc}$) is $\approx 204 \text{ km s}^{-1}$ (de Blok et al. 2008). The bar pattern speed for NGC 3627 is $\approx 55 \text{ km s}^{-1} \text{ kpc}^{-1}$ (Sheth et al. 2002), corresponding to $\approx 247 \text{ km s}^{-1}$ at this distance, yielding a net velocity of between the disk and the bar of $\approx 43 \text{ km s}^{-1}$. Thus, the propagation time is $\approx 3 \text{ Myr}$, less than the age of typical OB stars.

Another striking result from comparing the Enuc. 1 maps in Figure 2 is that the HCN and HCO^+ peaks are not co-spatial. The peak of the HCO^+ emission is located near the peak of the 33 and 94.5 GHz continuum emission. However, the HCN emission peaks in regions that surround the HCO^+ and continuum peaks. This may be the result in variations in the (dense) gas density, given that the critical density of HCN is nearly and order of magnitude larger than that of HCO^+ (e.g., Meier & Turner 2012). Stockpiles of ultra dense gas are likely still present in the immediate vicinity surrounding the newly formed HII region. Although, excitation effects may also be in play (e.g., see §3.3).

3.3. Dense Gas Fractions and Star Formation Efficiencies

In the top panel of Figure 5 we plot the dense molecular gas fraction against the estimated star formation efficiency for each region. The dense molecular gas fraction is taken to be the mass ratio of dense molecular gas traced by the $J = 1 \rightarrow 0$ transition of HCO^+ to the total molecular gas traced by the $J = 1 \rightarrow 0$ transition of CO. For this calculation we assume HCO^+ -to- H_2 and CO-to- H_2 conversion factors of $\alpha_{\text{HCO}^+} \approx 10 \text{ M}_\odot (\text{K km s}^{-1} \text{ pc}^2)^{-1}$ (e.g., Gao & Solomon 2004, we assume $\alpha_{\text{HCO}^+} \approx \alpha_{\text{HCN}}$) and $\alpha_{\text{CO}} \approx 4.3 \text{ M}_\odot (\text{K km s}^{-1} \text{ pc}^2)^{-1}$ (e.g., Solomon & Vanden Bout 2005; Bolatto et al. 2013), respectively. We only make use of the HCO^+ for deriving the dense molecular gas masses as we have data for all regions. The star formation efficiency (SFE), whose inverse is often referred to as the gas depletion time, is taken to be the ratio of the star formation rate (SFR) to the total molecular gas mass traced by the $J = 1 \rightarrow 0$ transition of CO. We converted the 33 GHz spectral luminosity into a star formation rate using the calibration for pure thermal emission given in (Murphy et al. 2011, 2012) and assumed an average 33 GHz thermal fraction of 79% (see §3.1). A clear trend of decreasing dense gas fraction with increasing star formation efficiency is observed. More specifically, the nuclear disk of NGC 3627 appears to have the largest fraction of its molecular gas in a dense phase, followed by the star-forming region at the end of the bar (Enuc. 2), and the isolated HII region (Enuc. 1). However, Enuc. 1 (the isolated HII region), appears to be converting its molecular gas into stars more efficiently (i.e., \approx a factor of 3 more rapidly) than either the star formation region at the end of the bar or the nuclear disk. By plotting the HCO^+ velocity dispersions from the fitted line profiles in Figure 3 against star formation efficiency in the middle panel of Figure 5, we find that the star formation efficiency for each region increases with decreasing velocity dispersion. Thus, perhaps unsurprisingly, the dynamical state of the dense gas appears to have a larger impact on the star formation process than the actual fraction of dense gas that is available for star formation.

Comparing the dense gas fraction and the efficiency of star formation on much larger scales, Usero et al. (2015) recently found systematic trends in both the dense gas fraction and the efficiency with which dense gas forms stars. That study included NGC 3627, though with a beam area two orders of magnitude larger than our study. Similar to our results, but using HCN, they found that in ≈ 30 disk galaxies, the apparent dense gas fraction increases by moving from the outer, low surface density parts of galaxies to the inner regions. At the same time, they found the apparent efficiency with which dense gas forms stars (for them, SFR/HCN) appears to decrease as one moves from the lower surface density disk to the inner parts of galaxies. They showed that these results could be explained by models of turbulent clouds (e.g., Krumholz & McKee 2005; Federrath & Klessen 2012) in which the average density and the turbulent Mach number in a cloud affect both the dense gas fraction and the ability of gas at different densities to form stars. Similar results have been found considering the apparently low rate at which dense gas forms stars in the central part of the Milky Way (e.g., Longmore et al. 2013; Kauffmann et al. 2013; Rathborne et al. 2014). With the improved resolution offered by ALMA, we are able to measure a velocity dispersion that may be more directly related to the turbulent velocity dispersion (at least outside the central region). The observation of variable dense gas efficiency (SFR/HCO^+) and suppressed star formation in the central, high dispersion part of the galaxy appears to agree at least qualitatively with these results.

Since we have relied on only the $J = 1 \rightarrow 0$ transition of HCO^+ to derive the dense gas mass, and have assumed similar conversion factors for HCN and HCO^+ to dense H_2 , it is illustrative to see how the HCN-to- HCO^+ line brightness ratio varies among regions. This is shown in the bottom panel of Figure 5, and plotted against star formation efficiency. The HCN-to- HCO^+ line brightness changes by a factor of ≈ 2 between both extranuclear star-forming regions over a similar change in star formation efficiency. This trend may be due to gas excitation effects given that the abscissa is a measure of the number of ionizing photons (free electrons) per unit molecular gas mass. For instance, as discussed in Papadopoulos (2007), the HCO^+ abundance is known to be sensitive to the ionization degree of molecular gas, which can significantly reduce the HCO^+ abundance in star-forming and highly turbulent molecular gas, while HCN remains abundant. Given the observed trend, this appears to be a plausible explanation. However, there are many alternative explanations for changes in the ratio of HCN-to- HCO^+ line brightness ratio including variations in gas density (see, e.g., Meier & Turner 2012). Given the large error bar on the line-brightness ratio for Enuc. 1, further speculation here is unwarranted. Regardless, it is worth pointing out that even if one ignores the large error bar, the trend observed in the top panel of Figure 5 would persist even if we instead used the HCN-derived dense gas mass.

4. CONCLUSIONS

In this paper we have combined ALMA/Band-3 line and continuum images with VLA/Ka-band images to characterize the star formation activity on ≈ 100 pc scales around three distinct regions within the nearby galaxy

NGC 3627; i.e., a nuclear disk hosting an AGN, an isolated HII region (Enuc. 1), and a star-forming complex at the end of a bar (Enuc. 2). Our conclusions can be summarized as follows:

- The thermal fraction at 33 GHz is nearly unity at the peaks of the HII regions as mapped on ≈ 100 pc scales, with an average value of $\approx 76\%$ for both extranuclear star-forming regions. The mean thermal fraction at 33 GHz among the three regions studied is 79% with a dispersion of 19%. We additionally found the radio spectral index to become both increasingly negative and positive away from the peaks of the HII regions, indicating an increase of extended non-thermal emission from diffusing cosmic-ray electrons and the possible presence of cold dust, respectively.
- The peaks of the $J = 1 \rightarrow 0$ HCN and HCO^+ line emission are spatially offset from the peaks of the 33 and 94.5 GHz continuum emission. For Enuc. 2, the continuum and gas are spatially offset in the plane of the sky by $\approx 3''$ (≈ 130 pc at the distance of NGC 3627). Assuming that the 33 and 94.5 GHz continuum is primarily powered by free-free emission, and that the $J = 1 \rightarrow 0$ HCN and HCO^+ line emission is tracing dense, UV-shielded gas, this indicates that our data reach an angular resolution at which one can spatially distinguish sites of current star formation from the fuel stockpiles for the next-generation of star formation.
- Combining our ALMA and VLA observations with archival BIMA CO ($J = 1 \rightarrow 0$) data, we calculate dense gas fractions and star formation efficiencies for each region, finding that the dense gas fraction decreases with increasing star formation efficiency. This suggests that an increase in the dense gas content of star-forming regions does not reflect an increased efficiency for which parts of galaxies can turn molecular gas into stars among the three, diverse regions studied here. Specifically, Enuc. 1 (an isolated HII region) appears to be converting molecular gas into stars more efficiently than both the star-forming region at the end of the bar or the nuclear disk. We additionally find that the velocity dispersion of the dense gas in each region decreases with increasing star formation efficiency, indicating that the dynamical state of the dense gas, rather than its abundance, plays a larger role affecting ongoing star formation activity.
- The $J = 1 \rightarrow 0$ HCN/ HCO^+ brightness ratio and star formation efficiency both vary by a factor of ≈ 2 between the extranuclear HII regions. We speculate that this may be due to an increase in the ionization degree of molecular gas for the star-forming region having a higher star-formation efficiency, which in turn reduces the HCO^+ abundance while HCN remains abundant. However, alternative explanations (e.g., variations in the gas density) may also be plausible.

We would like to thank the anonymous referee for useful comments that helped to improve the content and pre-

sentation of this paper. The National Radio Astronomy Observatory is a facility of the National Science Foundation operated under cooperative agreement by Associated Universities, Inc. This paper makes use of the following ALMA data: ADS/JAO.ALMA#2012.1.00456.S. ALMA is a partnership of ESO (representing its member states), NSF (USA) and NINS (Japan), together with NRC (Canada) and NSC and ASIAA (Taiwan), in cooperation with the Republic of Chile. The Joint ALMA Observatory is operated by ESO, AUI/NRAO and NAOJ. This research has made use of the NASA/IPAC Extragalactic Database (NED), as well as the NASA/IPAC Infrared Science Archive, both of which are operated by the Jet Propulsion Laboratory, California Institute of Technology, under contract with the National Aeronautics and Space Administration.

REFERENCES

- Bolatto, A. D., Wolfire, M., & Leroy, A. K. 2013, *ARA&A*, 51, 207
- Conway, J. E., Cornwell, T. J., & Wilkinson, P. N. 1990, *MNRAS*, 246, 490
- Cornwell, T. J. 2008, *IEEE Journal of Selected Topics in Signal Processing*, 2, 793
- de Blok, W. J. G., Walter, F., Brinks, E., et al. 2008, *AJ*, 136, 2648
- Dicker, S. R., Korngut, P. M., Mason, B. S., et al. 2008, in *Society of Photo-Optical Instrumentation Engineers (SPIE) Conference Series*, Vol. 7020, Society of Photo-Optical Instrumentation Engineers (SPIE) Conference Series
- Federrath, C., & Klessen, R. S. 2012, *ApJ*, 761, 156
- Filho, M. E., Fraternali, F., Markoff, S., et al. 2004, *A&A*, 418, 429
- Freedman, W. L., Madore, B. F., Gibson, B. K., et al. 2001, *ApJ*, 553, 47
- Gao, Y., & Solomon, P. M. 2004, *ApJS*, 152, 63
- Graciá-Carpio, J., García-Burillo, S., Planesas, P., & Colina, L. 2006, *ApJ*, 640, L135
- Haynes, M. P., Giovanelli, R., & Roberts, M. S. 1979, *ApJ*, 229, 83
- Helfer, T. T., Thornley, M. D., Regan, M. W., et al. 2003, *ApJS*, 145, 259
- Ho, L. C., Filippenko, A. V., & Sargent, W. L. W. 1997, *ApJS*, 112, 315
- Kauffmann, J., Pillai, T., & Goldsmith, P. F. 2013, *ApJ*, 779, 185
- Kennicutt, R. C., Calzetti, D., Aniano, G., et al. 2011, *PASP*, 123, 1347
- Kennicutt, Jr., R. C., Armus, L., Bendo, G., et al. 2003, *PASP*, 115, 928
- Klein, U., & Graeve, R. 1986, *A&A*, 161, 155
- Klein, U., Wielebinski, R., & Beck, R. 1984, *A&A*, 135, 213
- Klein, U., Wielebinski, R., & Morsi, H. W. 1988, *A&A*, 190, 41
- Kobulnicky, H. A., & Johnson, K. E. 1999, *ApJ*, 527, 154
- Krumholz, M. R., & McKee, C. F. 2005, *ApJ*, 630, 250
- Longmore, S. N., Bally, J., Testi, L., et al. 2013, *MNRAS*, 429, 987
- McMullin, J. P., Waters, B., Schiebel, D., Young, W., & Golap, K. 2007, in *Astronomical Society of the Pacific Conference Series*, Vol. 376, *Astronomical Data Analysis Software and Systems XVI*, ed. R. A. Shaw, F. Hill, & D. J. Bell, 127
- Meier, D. S., & Turner, J. L. 2012, *ApJ*, 755, 104
- Meier, D. S., Turner, J. L., & Hurt, R. L. 2008, *ApJ*, 675, 281
- Mezger, P. G., & Henderson, A. P. 1967, *ApJ*, 147, 471
- Moustakas, J., Kennicutt, Jr., R. C., Tremonti, C. A., et al. 2010, *ApJS*, 190, 233
- Murphy, E. J., Helou, G., Condon, J. J., et al. 2010a, *ApJ*, 709, L108
- Murphy, E. J., Condon, J. J., Schinnerer, E., et al. 2011, *ApJ*, 737, 67
- Murphy, E. J., Bremseth, J., Mason, B. S., et al. 2012, *ApJ*, 761, 97
- Murphy, T., Cohen, M., Ekers, R. D., et al. 2010b, *MNRAS*, 405, 1560
- Niklas, S., Klein, U., & Wielebinski, R. 1997, *A&A*, 322, 19
- Nikolic, B., & Bolton, R. 2012, *ArXiv e-prints*
- Pan, H.-A., Lim, J., Matsushita, S., Wong, T., & Ryder, S. 2013, *ApJ*, 768, 57
- Papadopoulos, P. P. 2007, *ApJ*, 656, 792
- Perley, R. A., & Butler, B. J. 2013, *ApJS*, 204, 19
- Rathborne, J. M., Longmore, S. N., Jackson, J. M., et al. 2014, *ApJ*, 795, L25
- Rau, U., & Cornwell, T. J. 2011, *A&A*, 532, A71
- Regan, M. W., Sheth, K., Teuben, P. J., & Vogel, S. N. 2002, *ApJ*, 574, 126
- Saintonge, A., Kauffmann, G., Kramer, C., et al. 2011, *MNRAS*, 415, 32
- Sault, R. J., & Wieringa, M. H. 1994, *A&AS*, 108, 585
- Sheth, K., Vogel, S. N., Regan, M. W., et al. 2002, *AJ*, 124, 2581
- Solomon, P. M., & Vanden Bout, P. A. 2005, *ARA&A*, 43, 677
- Turner, J. L., & Ho, P. T. P. 1983, *ApJ*, 268, L79
- . 1985, *ApJ*, 299, L77
- . 1994, *ApJ*, 421, 122
- Turner, J. L., Ho, P. T. P., & Beck, S. C. 1998, *AJ*, 116, 1212
- Usero, A., Leroy, A. K., Walter, F., et al. 2015, *ArXiv e-prints*
- Walter, F., Brinks, E., de Blok, W. J. G., et al. 2008, *AJ*, 136, 2563
- Zhang, X., Wright, M., & Alexander, P. 1993, *ApJ*, 418, 100